

## RESEARCH ON DYNAMIC RESPONSE OF SHALE UNDER SUPERCRITICAL CO<sub>2</sub> SHOCK FRACTURING

by

**Heng-Li ZHAI<sup>a,b</sup>, Cheng-Ming ZHAO<sup>c</sup>, Zhen-Hu LYU<sup>d</sup>,  
Ming-Sheng LIU<sup>a</sup>, Xu-Hao FAN<sup>a</sup>, Hai-Zhu WANG<sup>a\*</sup>,  
Bin WANG<sup>a</sup>, Qing-Li ZHU<sup>b</sup>, Yong-Gang YI<sup>d</sup>, and Zong-Jie MU<sup>a</sup>**

<sup>a</sup> State Key Laboratory of Petroleum Resources and Engineering,  
China University of Petroleum, Beijing, China

<sup>b</sup> Downhole Operation Company,  
Sinopec Shengli Petroleum Engineering Co., Ltd., Dongying, China

<sup>c</sup> CCDC Downhole Service Company, Chengdu, China

<sup>d</sup> Engineering Technology Research Institute,  
Petro China Xinjiang Oilfield Company, Karamay, China

Original scientific paper  
<https://doi.org/10.2298/TSCI2502575Z>

*This study conducted Brazilian splitting and shear tests on shale under various loading and shear rates, and performed numerical simulations of supercritical CO<sub>2</sub> shock stress evolution and impact damage. Results provide a theoretical foundation for efficient reservoir stimulation in unconventional reservoirs.*

Key words: *supercritical CO<sub>2</sub>, shock fracturing, loading rate, shear rate, stress wave, damage*

### Introduction

Supercritical CO<sub>2</sub> (Sc-CO<sub>2</sub>) shock fracturing is a novel technique that integrates Sc-CO<sub>2</sub> fracturing and explosive shock fracturing [1]. The process adds a pressure control valve to the fracturing string, which remains closed as liquid CO<sub>2</sub> is pumped and heated by the formation, transforming into compressible Sc-CO<sub>2</sub>. As a complex medium set with strong heterogeneity, rock exhibit elasticity, plasticity, and brittleness under varying loading conditions, influenced by loading state and history [2]. Studies, such as those by Zhang [3] on sandstone stress-strain behavior under dynamic loads, and Zhang *et al.* [4] on loading rate effects, confirm that dynamic conditions significantly impact rock strength. He *et al.* [5] further investigated the effects of confining pressure on stress wave propagation and rock strain using advanced dynamic testing and imaging techniques. Fan *et al.* [6] simulated stress wave propagation in fractured elastic media using the numerical manifold method. This study combined experiments and a strength calculation model to examine rock behavior under shock fracturing. A finite element-based stress wave propagation model was developed to investigate the evolution of tensile and shear stresses and rock damage characteristics under varying shock pressures.

\* Corresponding author, e-mail: whz0001@126.com

### Experimental of rock dynamic strength testing

Experiments used shale from the Longmaxi Formation outcrop in Sichuan as a representative unconventional reservoir rock. Brazilian splitting and shear tests were conducted at varying loading rates. Cylindrical shale specimens (25 mm × 50 mm for splitting, 50 mm × 50 mm for shear) underwent tensile and shear loading to induce failure, with dynamic strengths calculated from load data. A TAW-1000 servo system measured dynamic tensile and shear strengths while monitoring axial load variations. Tensile tests were conducted at loading rates of 0.1, 0.5, 2.5, 12.5, and 62.5 mm/s, while shear tests used rates of 0.1, 0.5, 2.5, 5.0, and 12.5 mm/s.

Figure 1 compares axial load and loading time curves at various loading rates. At loading rates of 0.1, 0.5, 2.5, 12.5, and 62.5 mm per minute, the maximum axial loads were 5.710 kN, 6.333 kN, 6.901 kN, 7.414 kN, and 7.883 kN, corresponding to tensile strengths of 10.00 MPa, 11.30 MPa, 12.09 MPa, 12.85 MPa, and 13.81 MPa, respectively. Shale tensile strength increases with loading rate, but the growth rate decreases from 13%-7.47%, indicating a stable dynamic tensile strength limit. Similarly, for shear rates of 0.1 mm, 0.5 mm, 2.5 mm, 5.0 mm, and 12.5 mm per minute, the maximum axial loads were 51.36 kN, 54.58 kN, 59.25 kN, 61.90 kN, and 63.87 kN, corresponding to shear strengths of 27.81 MPa, 29.56 MPa, 32.09 MPa, 33.53 MPa, and 34.59 MPa. Shale shear strength also increases with shear rate, with the growth rate decreasing from 6.29%-3.16%, suggesting a stable dynamic shear strength limit. Under high strain rates, both tensile and shear strengths increase, enhancing load-bearing capacity and strain energy accumulation.

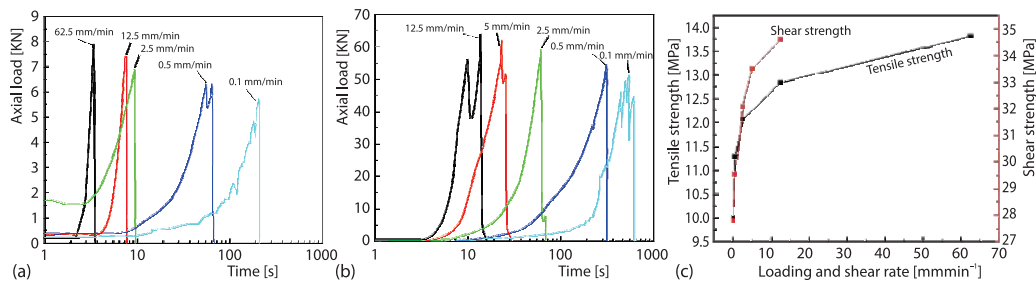


Figure 1. Loading curve; (a) tensile test; (b) shear test, and (c) dynamic intensity statistics

At present, the theory of rock strength changing with loading rate can be divided into  $J$  criterion and  $S$  criterion according to the strength curve of rock [7]. The  $J$  criterion requires less parameters, lower corresponding variability requirements, and easy determination. Therefore, this study investigates tensile and shear strengths under varying loading and shear rates based on the  $J$  criterion. Under the condition of  $J$  criterion, the static and dynamic strength of rock can be expressed:

$$\frac{\sigma_d}{\sigma_s} = \alpha + k_{\epsilon\alpha} \ln \left( \frac{\epsilon_d}{\epsilon_s} + 1 \right) \quad (1)$$

where  $\sigma_d$  is the dynamic tensile strength of rock at strain rate of  $\epsilon_d$ ,  $\sigma_s$  – the tensile strength of rock at strain rate of  $\epsilon_s$ , and  $\alpha$  and  $k_{\epsilon\alpha}$  are the rock constants independent of the loading rate. In addition, the calculation of shear strength is analogous.

To elucidate the functional relationship between shale's dynamic tensile strength and loading rate, the loading rate is transformed into a dimensionless logarithmic scale, with the  $y$ -axis representing non-dimensional tensile strength. Similarly, dynamic shear strength was an-

alyzed using the same method, as shown in fig. 2(a). An approximately linear relationship was observed between the dimensionless strengths and loading rate. Least squares fitting, incorporating static loading rate data and corresponding strengths, was employed to develop tensile and shear strength models for shale under arbitrary loading rates:

$$\sigma_d = 10 \times \left[ 1.0174 + 0.0569 \times \ln \left( \frac{\varepsilon_d}{0.1} \right) \right] \quad (2)$$

$$\tau_d = 27.81 \times \left[ 0.9915 + 0.0522 \times \ln \left( \frac{\varepsilon_d}{0.1} \right) \right] \quad (3)$$

Zhao [8] investigated wellbore pressurization under varying shock pressures and temperatures during Sc-CO<sub>2</sub> shock fracturing, correlating the pressurization rate with shale stress loading. Figure 2(b) illustrates the dynamic strength curves at 45 °C, showing that Sc-CO<sub>2</sub> shock fracturing increases shale tensile strength by 81.9%-90.52% and shear strength by 48.22%-56.13% compared to quasi-static loading. Moreover, at equal strain rates, shale shear strength exceeds tensile strength, indicating that tensile failure dominates under weaker impacts while shear failure prevails under stronger impacts.

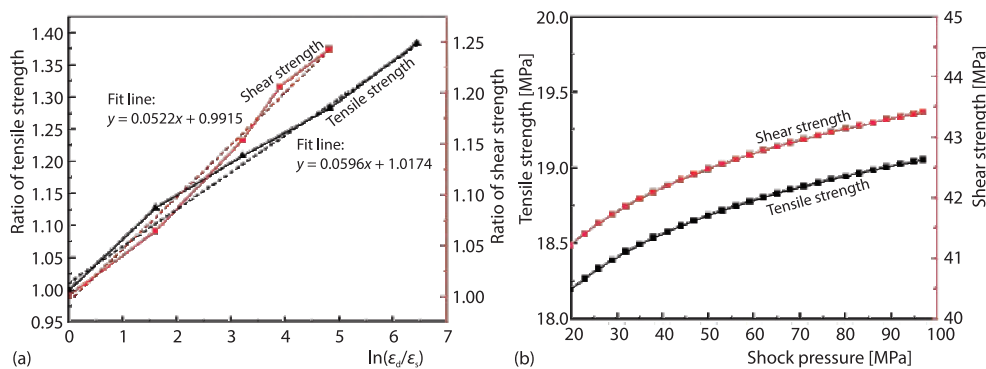


Figure 2. (a) Dimensionless relationship fitting and (b) tensile and shear strength distribution

### Numerical simulation of shock wave propagation and damage

In Sc-CO<sub>2</sub> shock fracturing, fracture development can be divided into two-stages [9, 10]:

- the stress wave failure stage, where the rock is initially damaged by a rapidly propagating stress wave and
- the fluid invasion stage, during which microfractures expand, coalesce, and propagate further as Sc-CO<sub>2</sub> invades the fractures.

This section focuses on the stress wave failure stage, analyzing the spatiotemporal distribution of tensile and shear stresses in shale under different shock pressures. By integrating established tensile and shear strength relationships, the study investigates stress wave-induced damage patterns to elucidate the damage mechanisms in Sc-CO<sub>2</sub> shock fracturing. Figure 3 presents a 2-D finite element model [11] of stress wave propagation in a 200 mm × 200 mm rock domain (with mechanical parameters based on experimental data) and a hole end size of 5 mm × 50 mm.

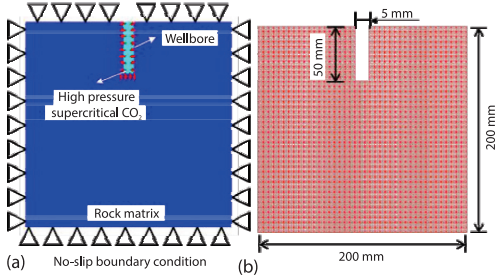


**Figure 3. Model settings: (a) physical and boundary conditions and (b) mesh division**

The research is a 2-D plane problem. Each element has 6 DoF. The displacement  $u$  of the element is expressed:

$$u = Na^e = N[x_1 \ y_1 \ x_2 \ y_2 \ x_3 \ y_3]^T \quad (4)$$

where  $u$  is the displacement vector of node,  $N$  – the shape function,  $a^e$  – the displacement component of each node, and  $x_1, x_2, x_3, y_1, y_2, y_3$  are the displacement in the  $x$ - and  $y$ -directions, respectively. The strain matrix of the element can be further obtained [11]:

$$\varepsilon = Lu = \begin{bmatrix} \frac{\partial}{\partial x} & 0 & \frac{\partial}{\partial y} \\ 0 & \frac{\partial}{\partial y} & \frac{\partial}{\partial x} \end{bmatrix}^T Na^e = Ba^e \quad (5)$$

where  $\varepsilon$  is the strain matrix,  $L$  – the differential operator matrix, converting displacement field into strain field, and  $B$  – the product of  $L$  and  $N$ .

Based on the constitutive equation of rock, the internal stress,  $\sigma$ , of rock is obtained:

$$\sigma = D\varepsilon \quad (6)$$

where  $D$  is the material stiffness matrix. It can be obtained:

$$D = \frac{E}{1-\nu^2} \begin{bmatrix} 1 & \nu & 0 \\ \nu & 1 & 0 \\ 0 & 0 & \frac{1-\nu}{2} \end{bmatrix} \quad (7)$$

where  $E$  is the elastic modulus of rock and  $\nu$  – the Poisson's ratio of rock.

Based on the principle of virtual work, construct the stiffness matrix:

$$\int_{\Omega} \delta\varepsilon^T \sigma d\Omega - \int_{\Omega} \delta u^T f d\Omega - \int_{\Omega\Gamma} \delta u^T \bar{t} d\Gamma = 0 \quad (8)$$

where  $\Omega$  is the surface domain,  $\Gamma$  – the surface boundary domain,  $\delta\varepsilon$  – the virtual strain of slight deformation,  $\delta u$  – the virtual displacement,  $f$  – the volume force acting on the interior of rocks, and  $\bar{t}$  – the surface forces acting on rock boundaries.

By substituting the imaginary position into the aforementioned formula, we can get:

$$\int_{\Omega} (\delta a^e)^T B^T DBa^e d\Omega - \int_{\Omega} (\delta a^e)^T N^T f d\Omega - \int_{\Omega\Gamma} (\delta a^e)^T N^T \bar{t} d\Gamma = 0 \quad (9)$$

Through simplification, we can get:

$$K^e a^e = F^e \quad (10)$$

$$K^e = \int_{\Omega} B^T DB d\Omega \quad (11)$$

$$F^e = \int_{\Omega} N^T f d\Omega + \int_{\Omega\Gamma} N^T \bar{t} d\Gamma \quad (12)$$

where  $K^e$  [ $\text{Nm}^{-1}$ ] is the element stiffness matrix obtained from discretization process and  $F^e$  – the equivalent external force acting on the node of the unit.

The local loading state and stress evolution of shale during stress wave propagation in Sc-CO<sub>2</sub> shock fracturing were analyzed. Under a 45 MPa shock pressure, as shown in fig. 4(a), shale near the borehole sides initially experiences compressive stresses over 40 MPa that attenuate outward, whereas at the borehole bottom, a lower shock (~23 MPa) induces tensile stresses exceeding the shale's tensile strength, triggering crack propagation. In contrast, the  $y$ -direction stress peaks at about 10 MPa, as shown in fig. 4(b). These results reveal that the borehole sides primarily undergo compression while the bottom experiences tension, explaining why failure usually initiates at the bottom, however, excessive shock pressure may crush the sides, compromising borehole stability, unlike conventional explosive fracturing, which typically damages the sides [12]. Tensile failure distribution was further examined using dynamic strength data. As shock pressure increases from 20-60 MPa, the tensile failure area expands downward from the borehole bottom, as shown in fig. 4(c). Above 40 MPa, tensile failure appears on the upper sides and laterally expands, with the tensile damage area ratio rising sharply from below 1%-8.8% at 60 MPa, as shown in fig. 4(d).

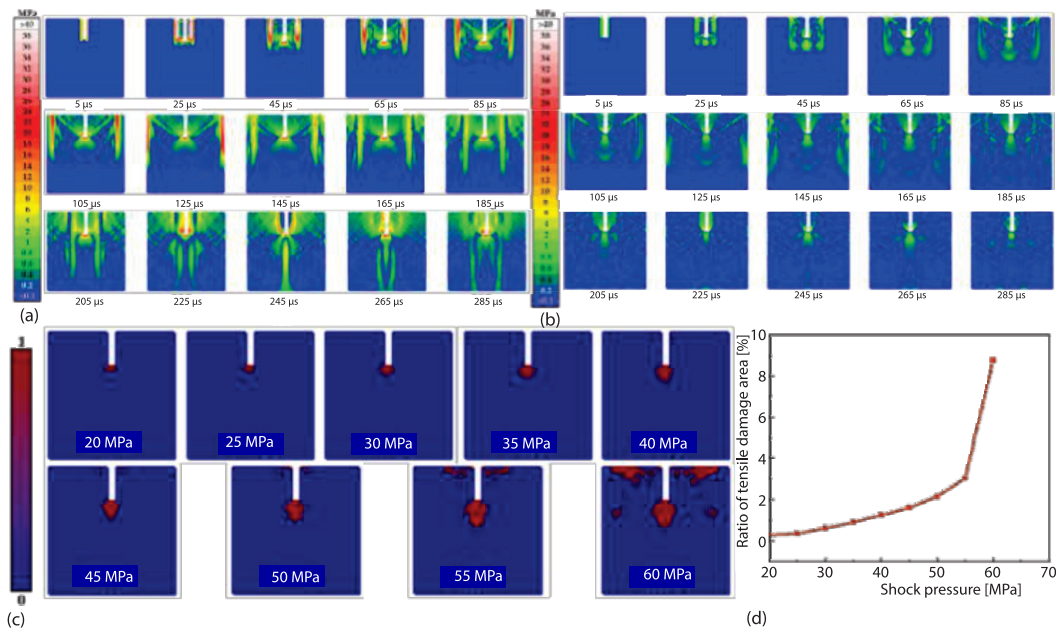


Figure 4. (a) The  $x$ -direction stress analysis, (b)  $y$ -direction stress analysis, (c) cloud map of tensile damage, and (d) proportion of tensile damage area

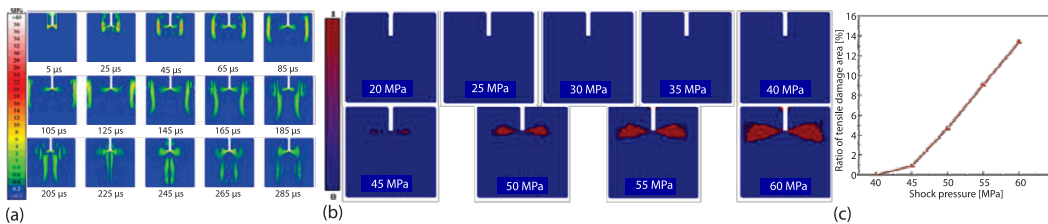


Figure 5. (a) Propagation of shear stress, (b) cloud map of shear damage, and (c) proportion of shear damage area

Shear stress propagation analysis under a 40 MPa shock pressure reveals a maximum shear stress of 30 MPa at the borehole bottom sides, which diminishes as it propagates outward, as shown in fig. 5(a). At stabilization, shear stress remains concentrated at these locations, indicating a high propensity for shear failure and fracture initiation. Shear failure area and distribution were further analyzed under varying shock pressures, as shown in fig. 5(b). No shear failure was observed below 40 MPa, while at 45 MPa, failure zones begin to form at the borehole bottom sides. With increasing shock pressure, these zones expand and localized failures emerge at the upper borehole, with the shear failure area rising from 0.9% at 45 MPa to 13.4% at 60 MPa, as shown in fig. 5(c).

### Conclusion

Compared to quasi-static loading, shale tensile and shear strengths increase under high strain rates, with stable maxima. Under Sc-CO<sub>2</sub> shock fracturing, tensile strength increases by 82%-91%, and shear strength by 48%-56%. Using the  $J$  criterion and least squares method, tensile and shear strength models were developed for shale under arbitrary loading and shear rates. During Sc-CO<sub>2</sub> shock, compressive stress dominates on both sides of the borehole, while tensile-shear stress dominates at the borehole bottom, facilitating fracture initiation. Shale failure is predominantly tensile under weak shocks, with shear failure gradually developing under strong shocks.

### Nomenclature

$a^e$  – displacement component, [m]  
 $D$  – material stiffness matrix, [Pa]  
 $E$  – elastic modulus, [Pa]  
 $u$  – displacement vector, [m]  
 $x_1, x_2, x_3, y_1, y_2, y_3$  – displacement, [m]

*Greek symbols*  
 $\sigma$  – stress, [Pa]  
 $\tau_d$  – dynamic shear strength, [MPa]  
 $\nu$  – Poisson's ratio, [-]

### Acknowledgment

This work is supported by the National Natural Science Foundation of China (No. 52341401, 52425402), International Cooperation and Exchange of the National Natural Science Foundation of China (No. 5241102279), and Science and Technology Development Project of the SilkRoad Economic Belt Innovation Zone, China (No. 2023L003005).

### References

- [1] Cong, R., et al., Feasibility on Exploitation of Coalbed Methane by SC-CO<sub>2</sub> Shock Fracturing (in Chinese), *Journal of China Coal Society*, 48 (2023), 8, pp. 3162-3171
- [2] Zou, C., et al., Change of Crack Mode in Rock Cracking Process under Quasi-Static and Dynamic Loadings, *Geomechanics and Geophysics for Geo-Energy and Geo-Resources*, 8 (2022), 2, pp. 1-23
- [3] Zhang, G., Propagation of Seismic Stress Wave and the Dynamic Response of Rocks (in Chinese), *Acta Seismologica Sinica*, 5 (1983), 4, pp. 477-482
- [4] Zhang, Z., et al., Effects of Loading Rate on Rock Fracture, *International Journal of Rock Mechanics and Mining Sciences*, 36 (1999), 5, pp. 597-611
- [5] He, C., et al., Research on Dynamic Response of Rock under Blast Loading and Active Confining Pressure (in Chinese), *Acta Armamentarii*, 38 (2017), 12, pp. 2395-2405
- [6] Fan, L., et al., Numerical Manifold Method (NMM) Simulation of Stress Wave Propagation through Fractured Rock Mass, *International Journal of Applied Mechanics*, 5 (2013), 2, 1350022
- [7] Gao, F., et al., Numerical Validation of Rock Mechanical Properties under Impact Loading (in Chinese), *Blasting*, 26 (2009), 2, pp. 1-14
- [8] Zhao, C., Rock Damage Mechanism Under Supercritical Carbon Dioxide Shock Loading (in Chinese), Ph. D. thesis, China University of Petroleum, Beijing, China, 2022

- [9] Cong, R., *et al.*, Supercritical CO<sub>2</sub> Shock Fracturing on Coal: Experimental Investigation on Fracture Morphology and Pressure Characteristics, *Proceedings*, 56<sup>th</sup> U.S. Rock Mechanics/Geomechanics Symposium, Santa Fe, N. Mex., USA, 2022
- [10] Agarwal, M., *et al.*, Comparing the Performance of Supercritical CO<sub>2</sub> Fracking with High Energy Gas Fracking in Unconventional Shale, *MRS Energy & Sustainability*, 9 (2022), 2, pp. 461-468
- [11] Mace, B., *et al.*, Modelling Wave Propagation in 2-D Structures Using Finite Element Analysis, *Journal of Sound and Vibration*, 318 (2008), 4, pp. 884-902
- [12] Fei, H., *et al.*, Study on Crushed and Fracture Zone Range under Combined Action of Stress and Detonation Gas (in Chinese), *Blasting*, 34 (2017), 1, pp. 33-36